Scilight

Journal of Innovations in Materials and Manufacturing Engineering
https://www.sciltp.com/journals/jimme

Article

Nondestructive Modular Leak Detection in 3D Printed 316L Stainless Steel Pipes via Laser Powder Bed Fusion

Jorge Avila [1,*], Eric MacDonald [2], David A. Roberson [1], Cesar Balderrama Armendáriz [3], Ana C. Martínez [1], Alexis Maurel [1], Sivasai Balivada [4], Miguel Hoffmann [5], Thomas Feldhausen [5] and Pedro Cortés [1]

[1] Metallurgical, Materials and Biomedical Engineering, University of Texas at El Paso, El Paso, TX 79968, USA
[2] Aerospace and Mechanical Engineering, University of Texas at El Paso, El Paso, TX 79968, USA
[4] Rapid Prototyping Laboratory (CAPA), Universidad Autónoma de Ciudad Juárez, Chihuahua 32310, México
[3] IBN Facility Imaging Core, University of Texas at El Paso, El Paso, TX 79968, USA
[5] Oak Ridge National Lab, Oak Ridge, TN 37830, USA
* Correspondence: jmavila9@miners.utep.edu

How To Cite: Avila, J.; MacDonald, E.; Roberson, D.A.; et al. Nondestructive Modular Leak Detection in 3D Printed 316L Stainless Steel Pipes via Laser Powder Bed Fusion. *Journal of Innovations in Materials and Manufacturing Engineering* **2026**, *1*(1), 5.

Received: 29 December 2025
Revised: 23 March 2026
Accepted: 26 March 2026
Published: 2 April 2026

Abstract: This research investigates the leak detection features of 316L Stainless Steel pipe structures manufactured via Laser Powder Bed Fusion (LPBF). This work involves the design of a modular sensor system integrating nondestructive evaluation (NDE) methods, including thermal imaging and ultrasonic frequency detection to detect and characterize leaks in components. This aims to improve leak detection sensitivity within medium-pressure gas systems, during continuous operation without halting flow or introducing safety risks. The system could be adaptable for use on unmanned aerial vehicles (UAVs), enabling remote leak detection in active environments. A custom pneumatic system incorporating temperature and pressure sensors was assembled to detect leaks in LPBF-printed 316L SS tee pipes. Experimental results and simulations confirm the system's effectiveness in leak detection and material evaluation. This research program also integrated a Python-based image recognition platform based on a metallography and optical microscopy to assess the porosity and complement the leak detection data on the printed structures. This allows a detailed analysis of pore distribution and internal leak paths, which could compromise structural integrity, critical for quality control during manufacturing. Findings suggest that the investigated approach holds potential for enhancing leak detection technologies and adapt them for advanced manufactured parts.

Keywords: additive manufacturing; nondestructive analysis; porosity; leaks; ultrasound

1. Introduction

Medium and high-pressure gas systems are critical for transporting gases and liquids across industries such as oil, aerospace, and energy [1]. These systems operate at high pressure conditions, requiring robust materials and advanced monitoring technologies to ensure safety and efficiency [2]. However, the complexity of these systems, particularly in aerospace applications, poses significant challenges for leak detection and maintenance [3]. Leaks in pressurized systems can lead to catastrophic failures, making early detection a high priority [4]. Traditional leak detection methods often require system shutdowns, which are costly and disruptive [5]. As a result, there is a growing demand for innovative solutions that can detect leaks in real-time without interrupting operations [6].

Additive manufacturing (AM), specifically laser powder bed fusion (LPBF), has emerged as a transformative technology for producing complex geometries, which are widely used in high-pressure systems [7]. LPBF enables

the creation of intricate designs with high precision, making it ideal for aerospace and industrial applications [8]. However, 3D-printed components, such as those made from 316L stainless steel (SS), can exhibit defects, including porosity and microcracks, which can compromise their integrity [9]. These defects require advanced nondestructive evaluation (NDE) techniques such as complex and time-consuming CT-analysis to evaluate their extent and consequently reliability of printed parts [10]. In contrast, the current research proposal addresses this need by developing a modular sensor system that integrates multiple NDE techniques to detect and characterize leaks in LPBF 3D-printed tee pipes. The modular sensor system is designed to operate under medium-pressure conditions (20–90 psi), providing real-time monitoring without requiring system shutdowns. By combining ultrasonic detection and thermal recognition techniques, the system provides a versatile solution adaptable to diverse applications including the aerospace field. Ultrasonic detection is particularly effective for identifying internal defects in materials, as ultrasonic waves can penetrate deep into structures [11]. However, traditional ultrasonic methods are often limited in their ability to detect small leaks in complex geometries [12]. To overcome this limitation, this research incorporates a custom electronic filter designed for the kHz frequencies generated by the pressure system. Additionally, thermal recognition techniques complement ultrasonic detection by identifying temperature variations caused by leaks [13]. When a gas leaks from a high-pressure system, it undergoes rapid expansion, resulting in a localized temperature drop [14]. This temperature change can be detected using infrared sensors, providing an additional layer of leak detection [15]. The integration of ultrasonic and thermal techniques in the modular sensor system ensures comprehensive leak detection, even in complex 3D-printed geometries [16]. This approach is particularly advantageous for industrial applications where the reliability of high-pressure systems is critical. In multiple industries, even minor leaks can have severe consequences, including system failures and safety hazards [17]. Traditional leak detection methods, such as visual inspections and pressure tests, are often inadequate for detecting small leaks in complex systems [18]. Moreover, these methods require system shutdowns, which are difficult to perform [19]. The modular sensor system presented in this research addresses these limitations by providing a non-intrusive solution that could operate continuously on any pipe network [20]. This capability could also be particularly valuable for unmanned aerial vehicles (UAVs), by providing them with lightweight and adaptable leak detection systems [21]. Indeed, UAVs equipped with a modular sensor system can perform remote inspections, reducing the need for human intervention and minimizing the risk of accidents. Early leak detection can prevent costly repairs and environmental damage, making this technology a valuable tool for the oil and gas industry [22]. The findings of this research have significant implications for the future of leak detection in pressure systems. By demonstrating the viability of 3D-printed components and advanced NDE techniques, this study paves the way for the development of more efficient and adaptable leak detection systems [23].

To validate the effectiveness of the proposed modular sensor, this research employs a custom pneumatic process that simulates leak conditions in 316L SS pipes that were 3D printed via LPBF. A previous testing set-up was investigated by Bayaniahangar et al. [24], where 3D printed ceramic components were placed in a customized pressurized chamber, and the leak was characterized in terms of flow rate. While Beyaniahangar et al. study is attractive to characterize leaks and address permeability of 3D printed components, the present research work proposes a concept in which no complex chambers are needed in order to detect leaks. Here, a modular sensor provides a versatile platform for pressurized systems in real-time. The sensor has a potential application beyond the aerospace sector, particularly in the oil and gas industry [25]. Pipelines in this sector are often located in remote and hazardous environments, making traditional inspection methods challenging and costly [26].

In addition to the leak testing, Python and image recognition techniques (enabled through metallography and optical microscopy) are used to analyze porosity in 316L SS parts produced via LPBF. This approach aids in assessing pore distribution and potential internal leaks to support the leak testing. The study highlights the importance of material characterization in ensuring the reliability of AM technologies [27]. By addressing the challenges associated with 3D printed components, this research could be expanded to support the adoption of AM in pressurized complex systems [28]. Furthermore, the development of advanced NDE techniques, such as those used in the modular sensor system, represents a significant step forward in nondestructive testing [29].

2. Materials and Methods

Twenty tee pipe specimens were fabricated via LPBF using a gas-atomized 316L stainless steel powder (Praxair TruForm Division, Indianapolis, IN, USA) with a particle size distribution of 15–45 μm (D10 = 18.2 μm, D50 = 32.7 μm, D90 = 43.5 μm) as measured by laser diffraction analysis. The components were designed in a SolidWorks CAD software (Dassault Systèmes, Vélizy-Villacoublay, France) with nominal dimensions of 2 inches (50.8 mm) in length and 1 inch (25.4 mm) in width (excluding flanges), featuring a 0.25 inch (6.35 mm) outer diameter and consistent 0.059 in (1.5 mm) wall thickness throughout the structure following NASA standards for

high pressure gas systems [30]. Fabrication was performed on an XACT Laser Powder Fusion Bed machine (Xact Metal XM200C printer, Indicate Technologies, Santa Clara, CA, USA) equipped with a 100W laser. The printing process parameters used in this work were based on the supplier's pre-set and is shown in Table 1.

Table 1. 3D printing process parameters used in this work on the Xact Metal XM200X.

Parameter	Hatchstyle Filling	Hatchstyle Support	Hatchstyle Outercontour
Laser focus (mm)	1	1	1
Laser power (W)	100	35	35
Laser speed (mm/s)	600	140	140

For microstructural characterization, representative samples were extracted from the tee pipe structures (straight section), and the grinding/polishing was performed on the samples until a mirror finish was reached. Chemical etching was performed using freshly prepared Marble's reagent consisting of 10 g $CuSO_4$ (ACS grade), 50 mL HCl (37% concentration), and 50 mL deionized H_2O, with immersion times empirically optimized between 15–30 s at controlled room temperature (23 °C ± 2) to achieve consistent etching results. Optical metallography was conducted using an Olympus GX53 inverted metallurgical microscope (Olympus Corp., Center Valley, PA, USA) equipped with a DP27 digital camera (20 MP resolution). For each sample, a minimum of 10 non-overlapping fields of view were systematically captured following a predefined grid pattern to ensure representative sampling of the microstructure.

Scanning electron microscopy was performed using a Hitachi TM-1000 SEM (Hitachi High-Tech, Schaumburg, IL, USA) operating with an accelerating voltage of 15 kV and employing backscattered electron (BSE) imaging. Energy-dispersive X-ray spectroscopy (EDS) was performed using the Hitachi TM-1000 tabletop scanning electron microscope equipped with an Oxford EDS detector (Oxford Instruments America, Concord, MA, USA). No EDS mapping was conducted; only area spectra were acquired.

For quantitative porosity analysis, a custom Python-based image processing program was developed using OpenCV libraries, implementing a multi-stage algorithm for automated void detection and characterization. The processing workflow first converts RGB micrographs to grayscale and applies contrast enhancement to improve void-to-matrix differentiation, followed by adaptive thresholding using Otsu's method to account for local intensity variations across the micrographs. The resulting binary images isolate dark regions corresponding to pores, after which morphological filtering is applied to remove noise and eliminate features below the spatial resolution limit of the imaging system (0.5 pixel ≈ 0.5 μm). Connected-component labeling is then used to identify individual voids, enabling their geometric characterization and ranking from largest to smallest based on area. Each detected pore is automatically enclosed within a green bounding box generated from its pixel connectivity and spatial extent, providing visual verification of the segmentation process while supporting quantitative analysis. The overall workflow consists of image loading, preprocessing, pore detection, sorting, and the generation of both visual annotations and quantitative porosity metrics for subsequent analysis.

Figure 1a,b shows optical pictures of the printed 316L T-pipe samples. Included in the picture is a representative batch of the samples manufactured in 45° with supports. To evaluate the leak-tightness of the fabricated 316L stainless steel pipe structures a custom pneumatic testing system was assembled incorporating both temperature and pressure monitoring capabilities, as seen in Figure 1c. The system utilized compressed air as the working medium and featured a pressure transmitter (±0.25% full scale accuracy) and a fast-response thermistor-based temperature sensor (±0.1 °C accuracy). Here, each sensor interfaced with a microcontroller-based data acquisition platform for real-time monitoring. The stainless-steel pipes were sealed and pressurized to 53 psi, with steady-state conditions maintained for 5 min to allow thermal and pressure stabilization. Leak detection on the pneumatic systems was based on monitoring the pressure decay and localized temperature profiles, indicative of microleak pathways or gas expansion effects.

In addition to pressure and temperature monitoring, thermal imaging was employed using two infrared cameras to visually detect localized cooling effects associated with air leakage, enhancing spatial resolution of leak sites. A FLIR A8580, a cooled MWIR HD camera (FLIR Systems, Wilsonville, OR, USA), was used to resolve small temperature contrasts associated with micro leaks, while a Fluke TC01C USB-C mobile camera (Fluke Corporation, Everett, WA, USA) was also used to investigate a modular system, based on low cost, and potentially drone compatible option for aerial inspections. Indeed, the thermal resolution of the Fluke camera limits the minimum detectable ΔT and leak size; however, it demonstrated the same thermal pattern and similar temperature readings than those recorded by the high end FLIR camera.

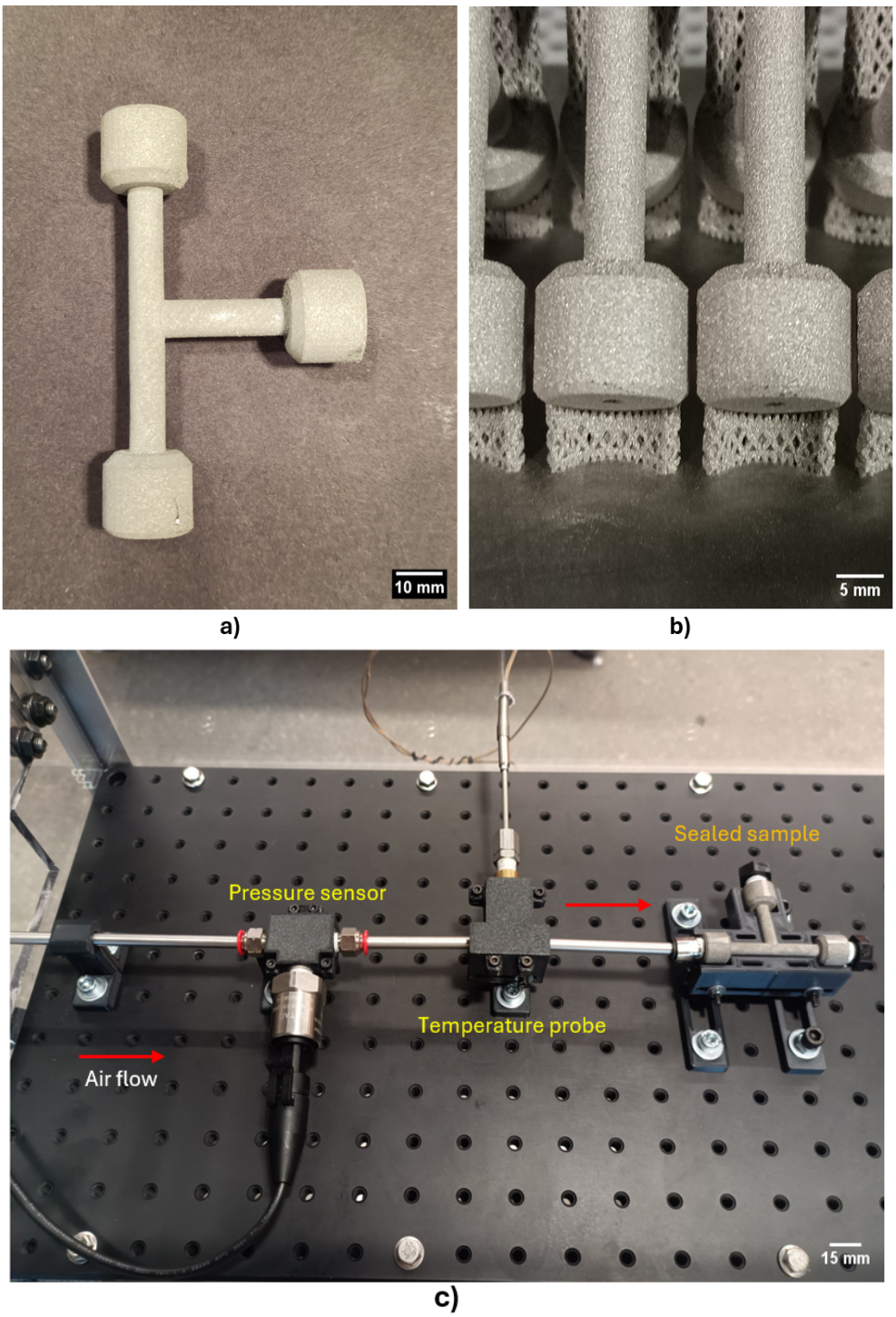

Figure 1. Printed parts and experimental set-up. (**a**) T-pipe sample without supports; (**b**) Sample batch of T-pipes; (**c**) Assembled pneumatic system to pressurize the samples.

In addition to thermal imaging, an airborne ultrasonic sensor was used to detect the acoustic signature of gas escaping through micro leaks. Unlike tracer gas or helium mass spectrometer methods, this approach does not require filling the part with a special gas and can operate with compressed air at 53 psi (with a max limit of 90 psi and a lower limit of 20 psi), which simplifies test logistics and is compatible with drone-based inspection.

As a final step, the printed samples were subjected to computed tomography (CT) scanning using a Bruker Skyscan 1276 CMOS system (Bruker Corporation, Billerica, MA, USA) to investigate the internal pore structure and assess porosity interconnectivity. This non-destructive imaging enabled three-dimensional visualization of subsurface voids and provided structural context for the leak detection results obtained from the infrared and ultrasonic sensing techniques.

Regarding the pore location and geometry, the tee pipes were fabricated using a layer-wise LPBF scan strategy combining hatch-based infill and dedicated contour scans to define the inner and outer free surfaces. This

separation between infill and contour regions could result in locally distinct thermal histories, particularly near free surfaces where reduced thermal mass and altered heat dissipation conditions influence melt pool stability and defect formation. Here, the lack of fusion defects tends to be irregular, with a probability to result in larger pore leaks. Indeed, presenting the scan strategy in conjunction with CT analysis establishes the processing context required to interpret the observed pore geometry, spatial distribution, and interconnected porosity discussed in the Results and Discussion section.

To further enhance the resolution and enable quantitative characterization of the pore population, additional high-resolution X-ray computed tomography (X-CT) analysis was performed using a Zeiss Xradia 620 Versa system (Carl Zeiss Microscopy GmbH, Oberkochen, Germany) at an isotropic voxel size of 17.7 μm, with imaging been done at 100 kV & 144 μA. The reconstructed volumes were obtained from 1601 projections, each averaged from three-1 s exposures, and processed using VGStudio Max 3.4 (Volume Graphics GmbH, Heidelberg, Germany). The VGEasyPore module was employed to extract volumetric defect features, including pore volume, equivalent diameter, and morphological descriptors such as sphericity. A filtering threshold was applied to exclude noise and ensure consistent defect segmentation. This higher-resolution dataset enabled statistical analysis of pore size distributions and spatial clustering, providing a quantitative basis for correlating porosity characteristics with the leak behavior observed experimentally.

3. Results and Discussions

The following section presents the experimental findings obtained from applying a multimodal nondestructive evaluation methodology to assess leak behavior, internal morphology, and structural integrity of 3D printed 316L stainless steel tee pipes. The performance and defect characterization of the components were related to the microscopy imaging. The integration of these complementary techniques enables a comprehensive correlation between manufacturing-induced features, defect formation, and leak pathways, providing a deeper understanding of the flaw-mechanics responsible for potential leakage in additively manufactured components.

3.1. Microscopy Analysis

Different 2D sections of the printed 316L stainless tee pipes were microscopically investigated to evaluate the degree of defects (as seen in Figures 2 and 3). It was observed that the body of the pipe presented a large degree of porosity, and in order to assess these defects, a void distribution analysis via Python Image Recognition was performed including a size frequency histogram. The analysis showed about 250 voids in total with 96.45% of the pores measuring below 25 μm, the majority (55.11%) falling under 5 μm. This distribution suggests that most voids are relatively small, which could indicate localized gas entrapment and/or lack of fusion. Larger voids (>50 μm) accounted for less than 2% of total porosity, and predominantly circular in shape. Studies by Sun et al. [31] have found that different processing conditions, such as laser power, scanning speed, or powder quality, can influence the pore size distribution. Smaller pores, as observed in our study, may have less impact on the bulk mechanical properties compared to larger, interconnected voids that could compromise material integrity [32].

A more representative defect analysis through different cross-sectional areas was also performed and it is shown in Figure 3. The figure displays both pore count and spatial distribution by applying the same image recognition methodology, the objective was not only to characterize void size distributions, but also to determine how porosity varies spatially and whether specific regions exhibit preferential defect accumulation linked to process induced phenomena.

Across the different metallographic sections analyzed, 2D image processing identified a large population of near surface voids distributed around the entire circumference of each sample. After segmentation and labeling, the samples exhibited between 62 and 160 individual voids per section, with pore sizes ranging from barely resolved micro-voids (<10 μm) to several larger defects exceeding ~100 μm. The voids showed a clear tendency to cluster near the inner and outer free surfaces, consistent with lack of fusion defects produced during contour scanning in LPBF processing. Although the precise area fraction varied slightly among images due to differences in local microstructure, the overall 2D porosity (area fraction) across the different sections was consistently in the range of 2.5–4.1%, indicating that the printed material contains a significant near surface pore population. These 2D results demonstrate not only the high density of discrete voids but also their non uniform spatial distribution, which is relevant for fluid transport and leak path formation in thin wall AM components. It is worth noting here that the green boxes outlined the identified defects, demonstrating the script's ability to accurately segment and classify these regions within the micrographs. This process allows for efficient identification of voids and provides a reliable tool for automated detection, improving the consistency and speed of the analysis.

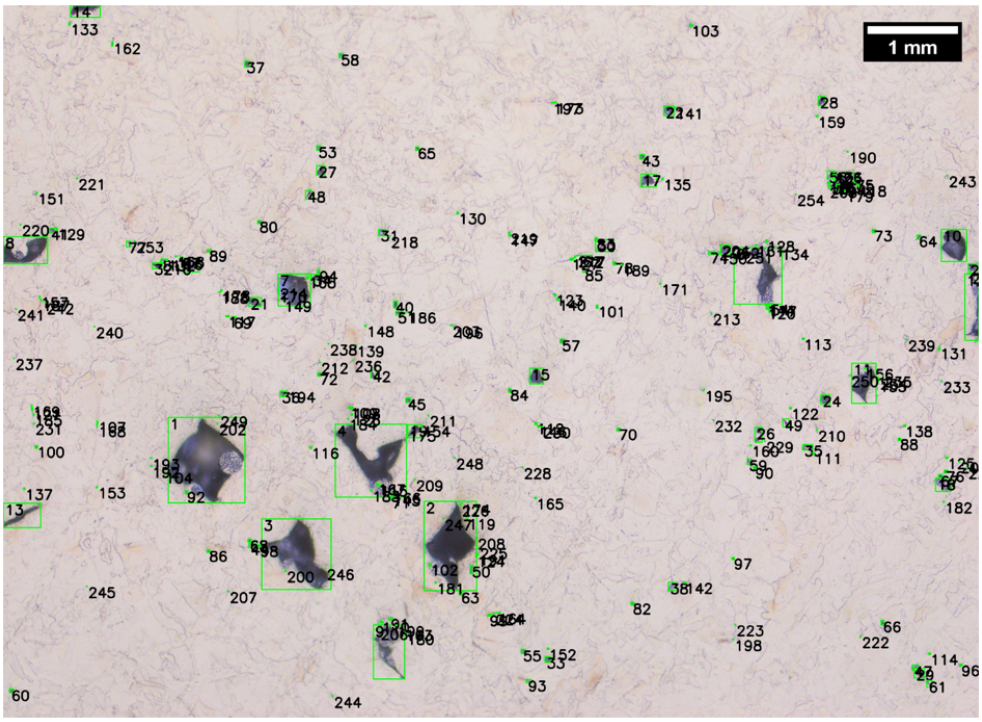

Figure 2. Representative void size and frequency of the printed specimens in a 2D image. Included in the figure is the printed steel pipe with highlighted sections (green boxes) where the microscopy analysis was performed.

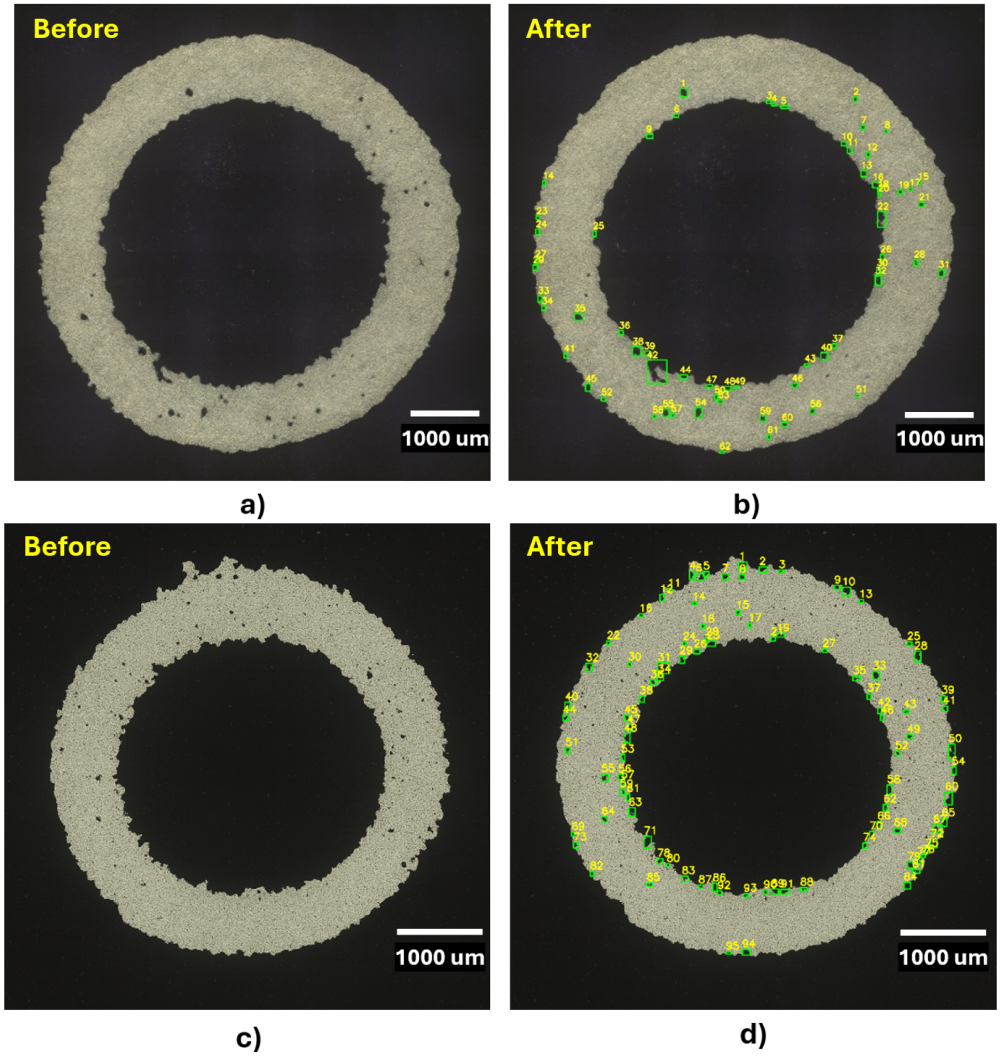

Figure 3. (**a**–**d**) 2D microscopic stitched images (before and after void analysis).

3.1.1. Pore Geometry and Formation Mechanisms

The pore population observed in the printed 316L stainless steel tee pipes exhibit distinct geometric features that provide insight into the underlying pore formation mechanisms during the LPBF process. The void size distribution, dominated by pores below 25 μm and primarily under 5 μm, suggests localized gas entrapment during rapid melt pool solidification, resulting in near-spherical micro-voids that are typically isolated [33]. In contrast, the larger and more irregularly shaped pores (>50 μm), predominantly concentrated near the inner and outer free surfaces, are characteristic of lack-of-fusion defects caused by insufficient local energy density and incomplete overlap between adjacent scan tracks or layers [34]. This near-surface accumulation is consistent with contour scanning effects, where reduced thermal mass and altered heat dissipation led to increased melt pool instability and incomplete fusion. The coexistence of spherical gas-related pores within the bulk and irregular lack-of-fusion pores near the surfaces indicates that multiple defect formation mechanisms are active simultaneously, and the spatial clustering of larger pores near free surfaces increases the likelihood of pore coalescence, promoting the formation of preferential leak pathways in thin-wall additively manufactured components. Reduction of porosity could be addressed by increasing the laser power, decreasing the hatch spacing and the layer thickness and optimizing the scan speed to enhance the volumetric energy density as mention before by Sun et al. [31].

3.1.2. Porosity Thresholds and Interconnected Pore Formation

The measured 2D porosity values, consistently ranging between approximately 2.5 and 4.1% across the analyzed sections, provide important insight into the transition from isolated pores to interconnected pore networks in the LPBF-fabricated components. At lower porosity levels, pores tend to remain discrete and spatially separated, limiting their impact across the wall thickness; however, as porosity approaches the upper bound of this range, the probability of pore interaction and coalescence increases significantly. This behavior is supported by the CT observations presented in Section 3.5, which reveal continuous subsurface pore coalescence spanning from the inner to the outer surfaces of the pipe wall. Such interconnected porosity indicates that a critical pore fraction threshold has been exceeded, enabling percolation pathways that facilitate gas leakage. While the exact percolation limit depends on local pore geometry and spatial distribution, the combined microscopy, CT, and leak testing results suggest that maintaining a low degree of porosity is required to prevent coalescence across pores to ensure leak-tight performance in thin-wall additively manufactured structures. Work performed by Huang et al. [35] has suggested the incorporation of a pore distribution factor (m) for predicting the percolation threshold. This distribution factor (m) is defined as the number of sites occupied by the pores generated each time on X-Y framed dimensional arrays. While the prediction of the percolation threshold is outside of the scope of this work, an imaging analysis in a per-layer fashion could provide representative data of the sites occupied by the pores to calculate an approximate threshold.

3.2. Scanning Electron Microscopy and Energy Dispersive Spectroscopy Analysis

A scanning electron microscopy (SEM) analysis was also carried out on the printed parts (see Figure 4a,b), and it confirmed the presence of micron-scale voids suggesting localized gas entrapment or incomplete melt consolidation. An energy dispersive spectroscopy (EDS) analysis (Figure 4c) was also performed on the printed samples validating the composition of alloying elements (Fe, Cr, Ni, and Mn) in the sampled regions along with minor traces of sulfur and silicon. Although, they remained within expected tolerances based on the Certificate of Analysis & Certificate of Conformity for the TruForm 316-3 from Linde. No significant inclusions or contamination particles were identified, affirming the quality of the feedstock and the inert build environment. EDS analysis clearly supported these observations, by displaying consistent elemental distribution across the layers, without any significant variations in alloy composition.

In addition to point-based EDS analysis, the elemental mapping of the leak-affected cross section revealed a homogeneous spatial distribution of Fe, Cr, Ni, Mo, and Mn across the analyzed region, with no evidence of compositional segregation associated with the observed voids. The elevated carbon and oxygen signals detected near the surface are attributed to sample preparation and surface oxidation effects rather than intrinsic alloy variation. The absence of localized compositional enrichment near pore boundaries indicates that the defects originate from the processing-related phenomena.

EBSD imaging shows small equiaxed grains near the lack of fusion areas due to a faster localized cooling rate and heterogenous nucleation caused by the presence of partially melted powder particles.

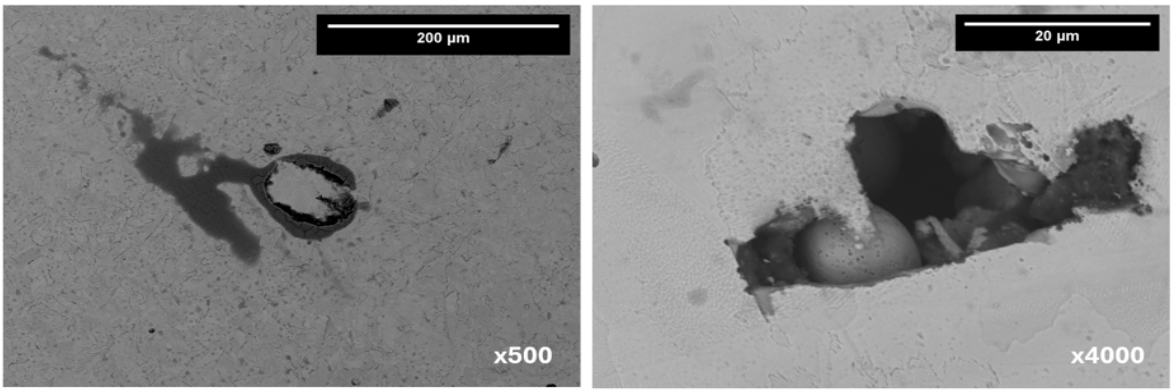
200 µm
x500
20 µm
x4000

a) b)

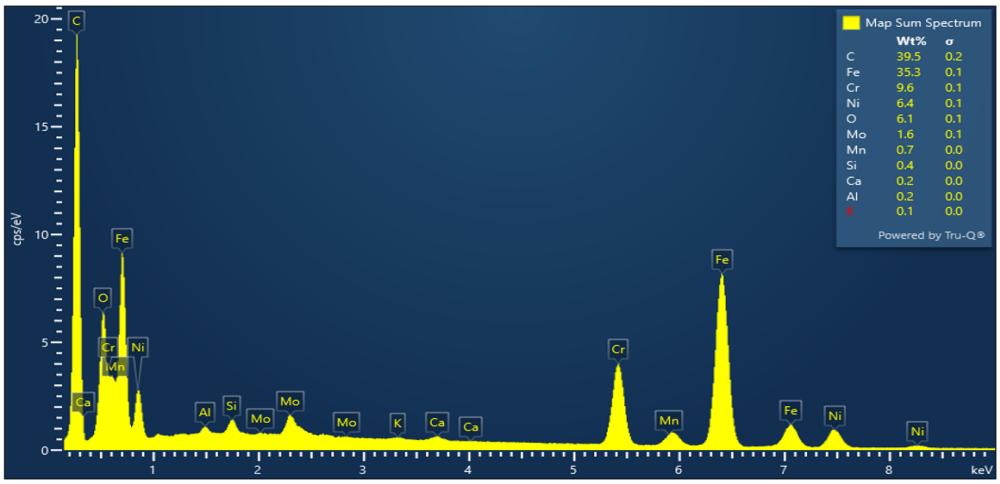
Map Sum Spectrum
Wt% σ
C 39.5 0.2
Fe 35.3 0.1
Cr 9.6 0.1
Ni 6.4 0.1
O 6.1 0.1
Mo 1.6 0.1
Mn 0.7 0.0
Si 0.4 0.0
Ca 0.2 0.0
Al 0.2 0.0
K 0.1 0.0
Powered by Tru-Q®
cps/eV
keV

c)

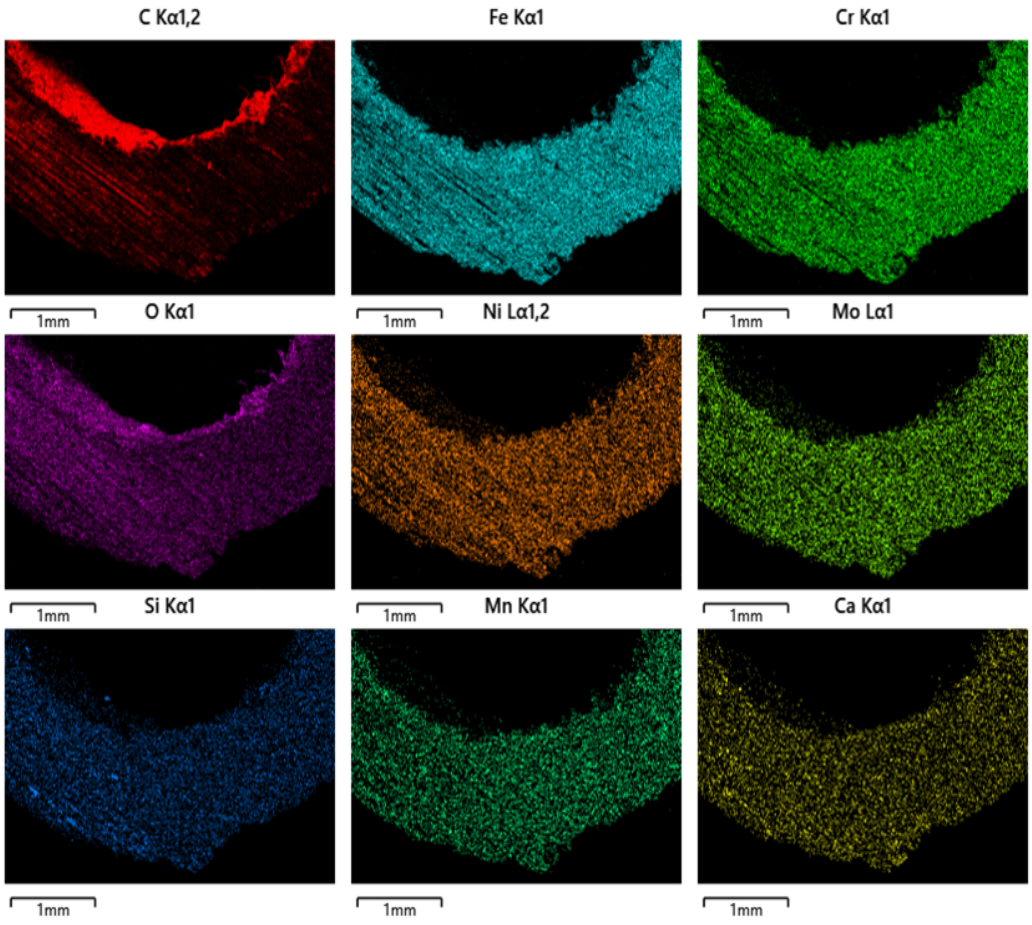
C Kα1,2
Fe Kα1
Cr Kα1
O Kα1
Ni Lα1,2
Mo Lα1
Si Kα1
Mn Kα1
Ca Kα1
1mm

d)

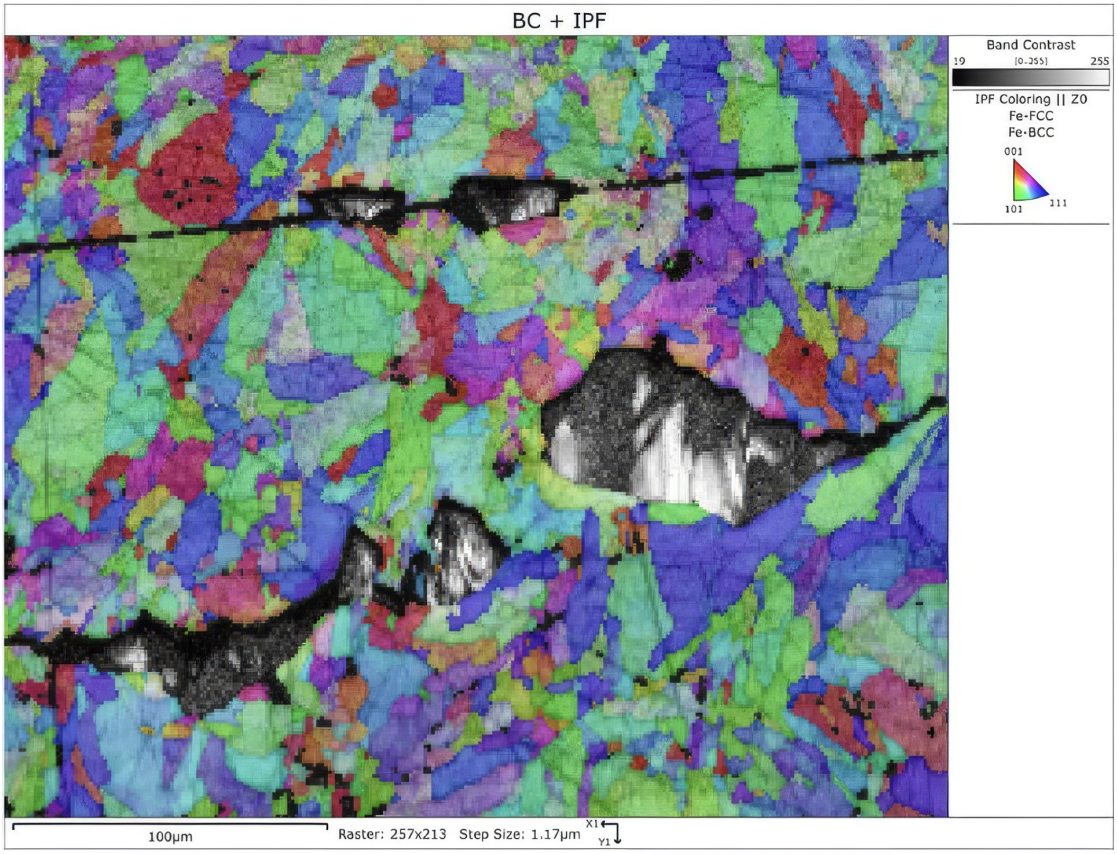

e)

Figure 4. (**a**) SEM Sample morphology with defect; (**b**) Lack of fusion void; (**c**) Representative EDS spectrum of the printed samples; (**d**) EDS mapping of sample; (**e**) EBSD of cross sectioned area.

3.3. Thermal Imaging

Leak tightness evaluation using the custom pneumatic testing rig revealed a significant through-wall leak present in all the LPBF fabricated tee pipe specimens. Notably, the major leak was consistently located in the same geometric region across all the samples with leak, near the 90° branch, indicating that this major defect might be associated with the inclusion of sharp angles [36]. To further verify the leak's location and ensure the reliability of the findings, additional nondestructive testing methods were employed. Thermal imaging and ultrasonic sensing played a critical role in corroborating the location and presence of this leak by providing independent confirmation.

Prior to thermal imaging, all samples were carefully cleaned to remove dust and surface contaminants that could influence emissivity or produce measurement artifacts. Emissivity control and thermal calibration procedures were performed for the imaging systems used in the study. Here, the emissivity settings and calibration routines were applied in accordance with the technical manuals and adjusted to match the metallic surface condition of the samples. This ensured that temperature readings reflect true thermal emission characteristics of the material rather than surface reflectivity or sensor variation, thereby improving the reliability of the thermal measurements of both camera platforms. FLIR images of the sample are shown in Figure 5, highlighting the thermal behavior before and after the application of airflow. In Figure 5a, the temperature field appears uniform, with no evident cold anomalies across the structure. However, in Figure 5b, once the airflow is introduced, a pronounced dark-blue region becomes visible within the red marked area, corresponding to a temperature of approximately 18.18 °C, which clearly indicates the presence of a leak. The sharp contrast between the surrounding warmer tones and the localized cold spot is a direct result of the high gamma settings used during the thermal capture, which enhance small temperature gradients and improve defect visibility. These details allow for precise identification of the leak path.

The underside section was also IR recorded during the air-testing and no presence of leak was detected on this section of the structure. This suggests that the presence of pores over-passed the percolation threshold, probably due to 90-degree shape. The presence of a sharp 3D printing angle can induce local stresses [37]. Indeed, either further optimization of printing process parameters or a wall-thickness enlargement in this section could provide a solution to the leak. For this specific work, the presence of a leak was well aligned with the goals of this

work, since this research effort seeks to detect leaks, rather than optimizing designs and/or processing parameters to avoid leaks on structures. Future modular NDE systems could confirm the presence of a single or multiple leak zones.

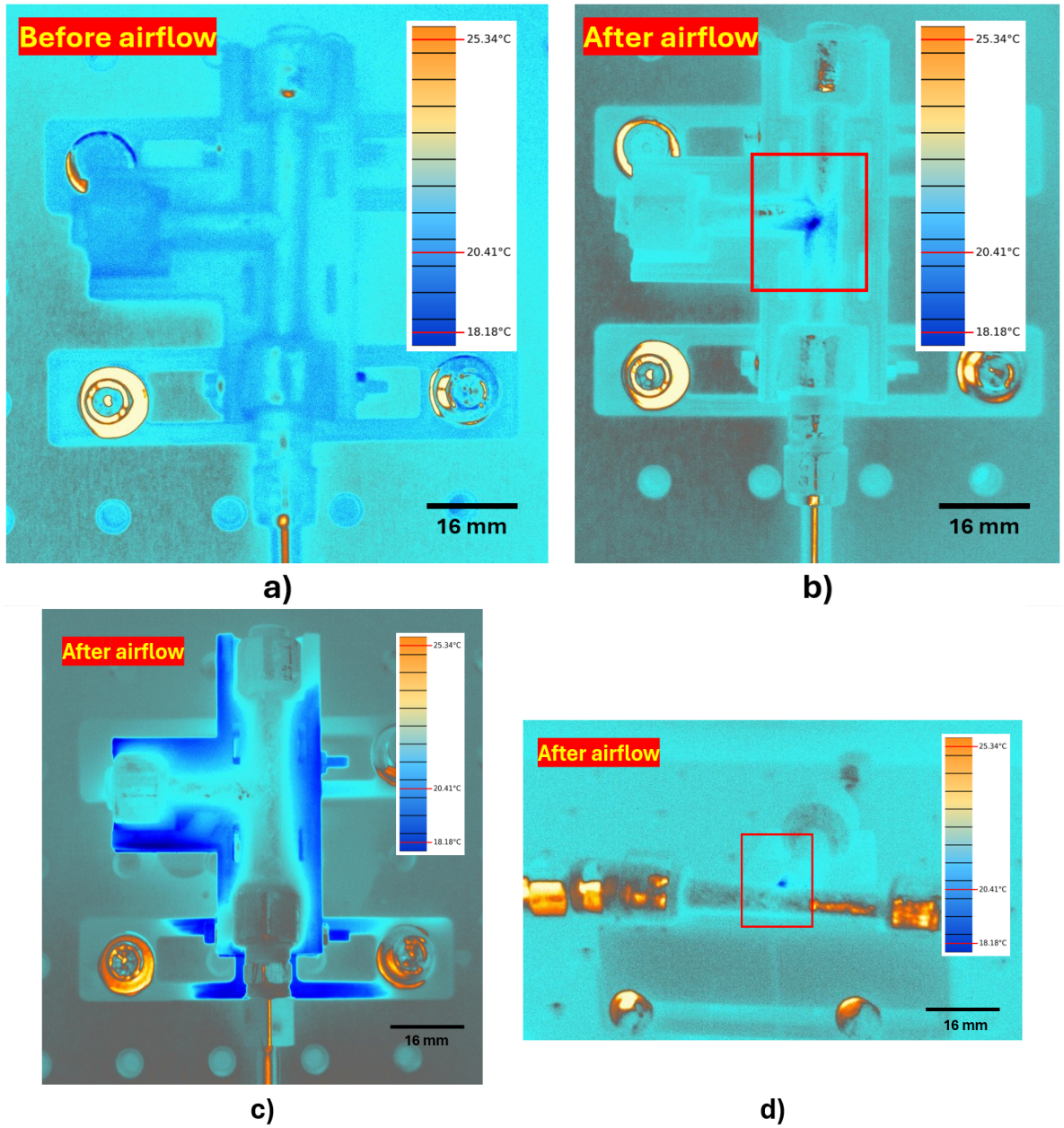

Figure 5. FLIR thermographic images showing leak detection (top, underside and side views) (**a**) Top view before airflow; (**b**) Top view after airflow; (**c**) Underside view after airflow, d) Side view after airflow.

Fluke thermal images of the assembly are shown in Figure 6, comparing the temperature field before and after airflow. In Figure 6a, the distribution is uniform, with no cold anomalies and a reference temperature of about 25.4 °C. After the airflow is introduced (Figure 6b), a clear cooling region appears within the highlighted area, reaching approximately 20.3 °C, indicating the presence of a leak or airflow disturbance. The high contrast palette of the Fluke camera enhances this temperature drop, making the defect easily identifiable. From the thermal readings of both cameras, the temperature difference of 2.24–3.5 °C remains acceptable when considering the gamma and calibration differences of each device. This highlights the advantage of smaller, lightweight cameras, which are ideal for drone inspections where bulky equipment is impractical. Despite their compact size and lower cost, these cameras still provide comparable resolution and reliable thermal contrast, making them an efficient and cost-effective alternative for field applications.

To further evaluate the robustness of the proposed nondestructive methodology under varying manufacturing conditions, additional specimens were fabricated and tested. First, a modified LPBF parameter set was implemented based on recent literature recommendations for improving melt pool stability and interlayer bonding

in 316L stainless steel [38]. The modifications included reducing the infill laser focus (1 mm to 0.5 mm), increasing contour laser power (35 W to 80 W), and adjusting its scan speed (140 mm/s to 250 mm/s). Thermal imaging of this specimen (Figure 6c) revealed no localized cold anomaly after airflow was introduced, indicating the absence of through-wall leakage under identical testing conditions.

In addition, a second specimen was fabricated using the original parameter set but with an increased wall thickness of +1 mm to evaluate the influence of geometric reinforcement on leak formation. The corresponding thermal image (Figure 6d) likewise showed a uniform temperature field without localized cooling during airflow. These results demonstrate that both process optimization and increased wall thickness effectively suppress pore interconnectivity responsible for leakage, and further confirm the sensitivity of the proposed nondestructive platform in discriminating between defective and defect-mitigated components.

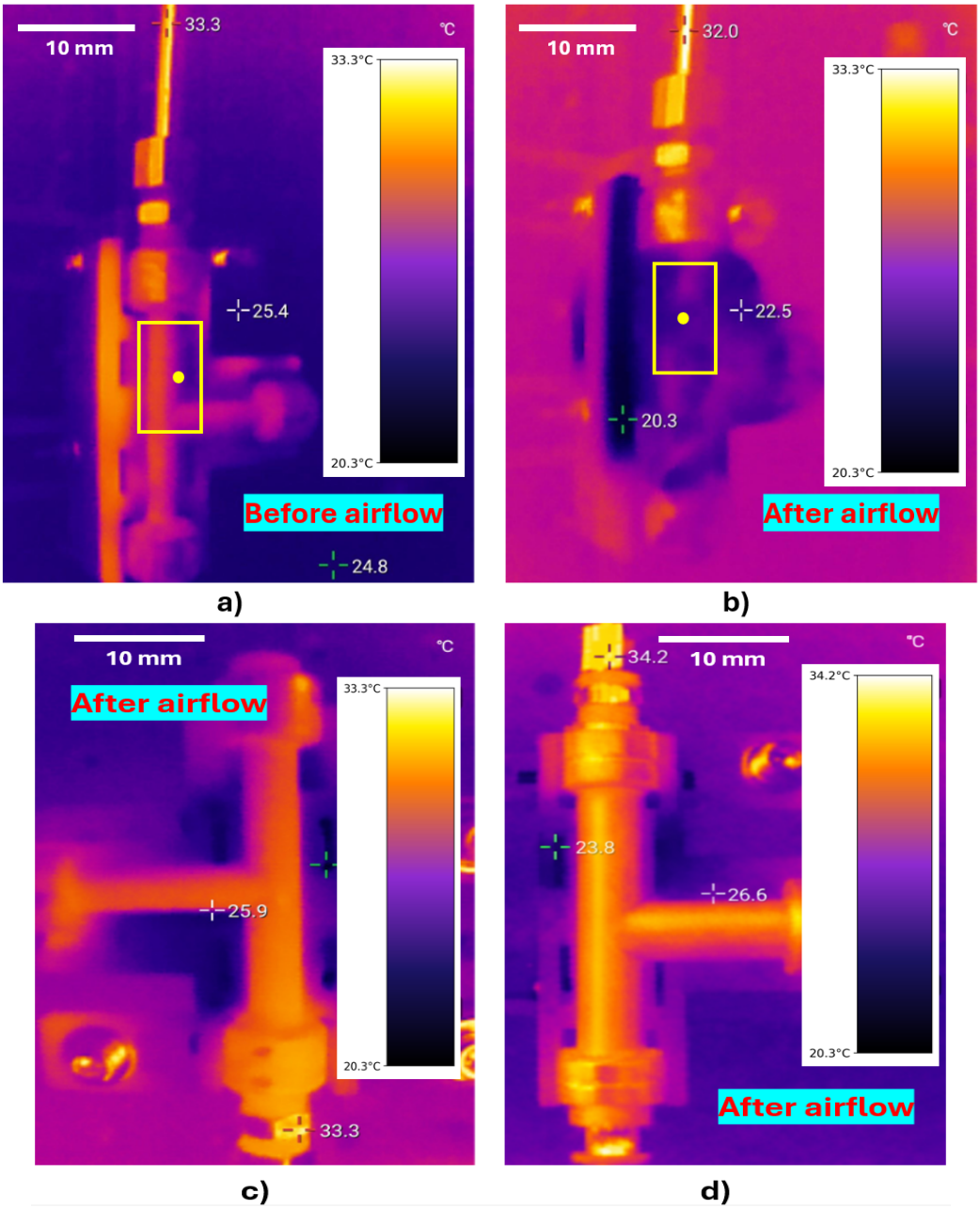

Figure 6. Fluke thermal images, (**a**) Baseline sample before airflow; (**b**) Baseline sample after airflow; (**c**) New parameter sample after airflow; (**d**) Thick sample after airflow**.**

3.4. Ultrasonic Frequency Detection

In addition to the thermal imaging approach, a custom ultrasonic frequency detector was designed, manufactured, and employed to further verify the presence and consistency of the leak. This custom-built sensor

operates within the 0–40 kHz range, allowing it to detect high-frequency sound waves [39], typically emitted by pressurized air escaping through microdefects.

The detector provides a threshold amplitude analysis with frequency measurement accompanied by a LED color status. The color indication provides a straight forward detection method: a green LED signals the absence of ultrasonic emissions, confirming no active leak, while a red LED indicates the presence of a leak. In terms of data collection, this was retrieved through a micro controller and processed with Python to obtain the different peaks of intensity on a time scale (dB vs. time), with a threshold set at −30.4 dB to classify leak vs. no-leak conditions. experimentally established by testing a control sample (without leaks). The threshold of –30.4 dB was selected based on the lower pressure limit of 20 psi, where signals consistently fell between –28 and –29 dB, distinguishing them from random noise. Meanwhile, the non-leaking sample remained at approximately –40 dB, confirming that readings below this threshold corresponds purely to background noise, even when testing up to the maximum 90 psi.

All leak detection experiments were performed on twenty T-pipes (four batches × five parts each). This allowed assessing both build to build variability (between batches) and part to part repeatability within each batch. Of all these parts, 18 samples presented leaks with no false positives (FP) or false negatives (FN) as seen in Table 2.

Table 2. Sample leak confirmation.

Status	No leak	Leak
Actual no leak	2 (TN)	0 (FP)
Actual leak	0 (FN)	18 (TP)

A representative decibels plot is shown in Figure 7, where the ultrasonic leak signal was analyzed in the frequency domain. The dominant component during leakage occurred between 3.0–3.3 kHz, while the non-leaking state remained below the −30.4 dB threshold. Leak detection was based on the signal-to-noise ratio (SNR). Without pressure the level remained near −40 dB. Once the system was pressurized, the intensity level reached approximately −26 dB, resulting in an SNR of ≈14 dB. During the leak detection, the highest peak showed a value of −25.56 dB associated with 3120 Hz, and the lowest a value of −26.33 dB with a 2660 Hz dominant frequency, as shown in Table 3.

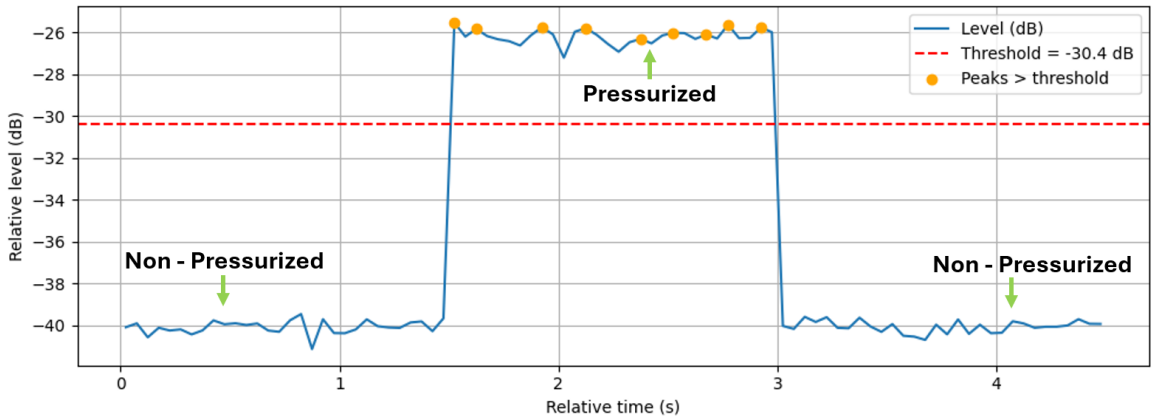

Figure 7. Representative leak detection dB vs. relative time. The plot shows in the threshold and pressurization and depressurization stages.

Table 3. Detected peaks above threshold.

Peak	Time (s)	Level (dB)	Dominant Freq (Hz)
1	1.525	−25.56	3120
2	1.625	−25.85	3180
3	1.925	−25.77	2800
4	2.125	−25.81	3220
5	2.375	−26.33	2660
6	2.525	−26.04	2960
7	2.675	−26.12	2980
8	2.775	−25.65	3240
9	2.925	−25.78	3100
Mean	2.275	−25.88	3028.89
Standard Deviation	0.5044	0.242	197.77

Figure 8 shows the acoustic signal during airflow in a sample without leaks. Here, the measured acoustic level remains well below the leak threshold of −30.4 dB throughout the entire 5 s interval, with fluctuations centered around −40 dB, indicating only background noise and structural vibration response to internal pressure. This baseline response establishes the reference condition for leak free parts and validates the acoustic method's ability to detect leaks.

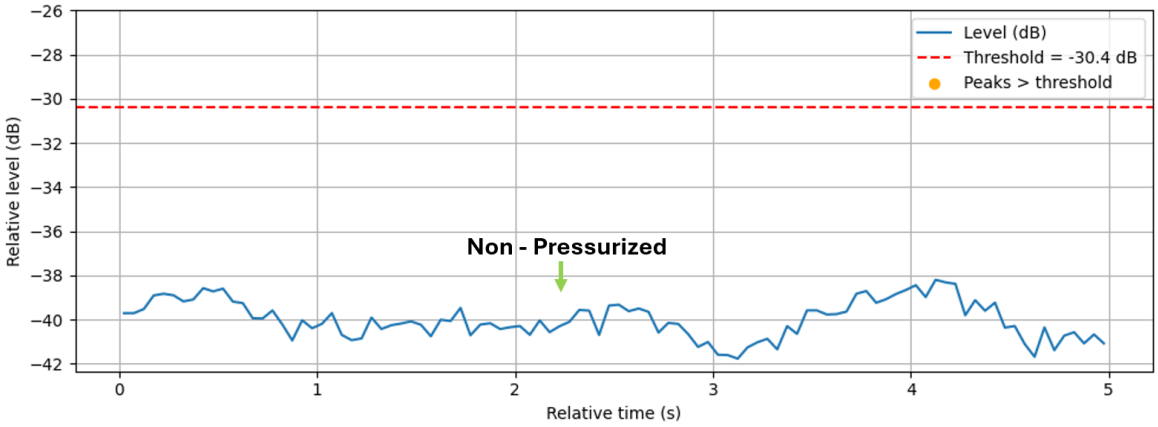

Figure 8. Leak detection profile of a sample with no leaks (dB vs. relative time).

By continuing the characterization of the leaks, a sample without leaks was used to incorporate three 1mm diameter orifices, to elucidate the dimension of the leaks presented on the printed sample. It was observed that the 1 mm orifice showed −20.23 dB, while 2 and 3 orifices resulted in −16.78 dB, and −12.57 dB respectively. Assuming a power-law relationship between leak diameter and sound intensity, a regression of intensity versus diameter was used to estimate an equivalent circular leak diameter for the 3D printed micro leaks. The measured average acoustic level of the micro leaks (−25.88 dB) corresponds to an equivalent diameter of approximately 0.4–0.5 mm.

The dominant frequency band (approximately 3.0–3.3 kHz) remained relatively consistent across the tested orifice sizes, indicating that leak size estimation is primarily governed by amplitude variation rather than frequency shift within the examined pressure range. Although interconnected lack-of-fusion pores may introduce increased flow turbulence compared to smoother keyhole-type defects, the present ultrasonic methodology is principally sensitive to effective leak area. Differentiation between pore morphology types would require higher-resolution spectral analysis and controlled morphology-specific experiments, which are considered for future work.

Following the acoustic analysis of the printed samples with leaks, a pressure decay study was performed on all the printed samples with leaks. Figure 9 shows 10 samples tested, where the system was pressurized at ~53 psi, and after the pressurization, the source was closed and the pressure decay in the samples was monitored. As observed in Figure 9, all samples displayed an exponential decay over time, reaching a gauge pressure of zero in about 80 s. The difference across profiles seems to be related to the degree of porosity on each individual sample. Here, a slower decaying might be associated with a restricted or fragmented gas pathway, while steeper drops indicate a larger interconnected leak.

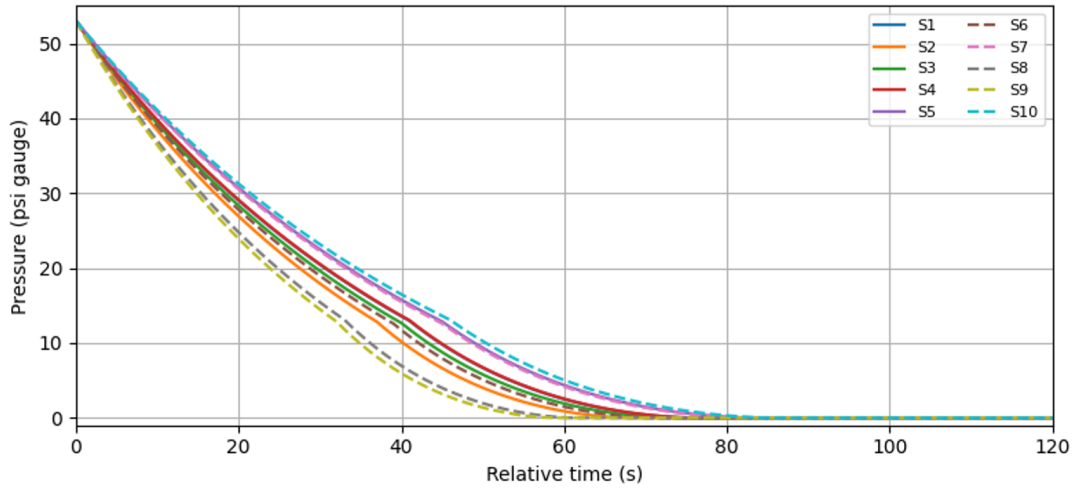

Figure 9. Pressure decay comparison of ten printed samples with leaks.

Subsequent to the characterization of the pressure decay, the leak rate was calculated as a function of the pressure (see Figure 10). As expected, leak rate decreases with decreasing gauge pressure., and different samples exhibit slightly different slopes corresponding to the variability in the leak area. The leak rate drops toward zero as the system pressure approaches atmospheric conditions.

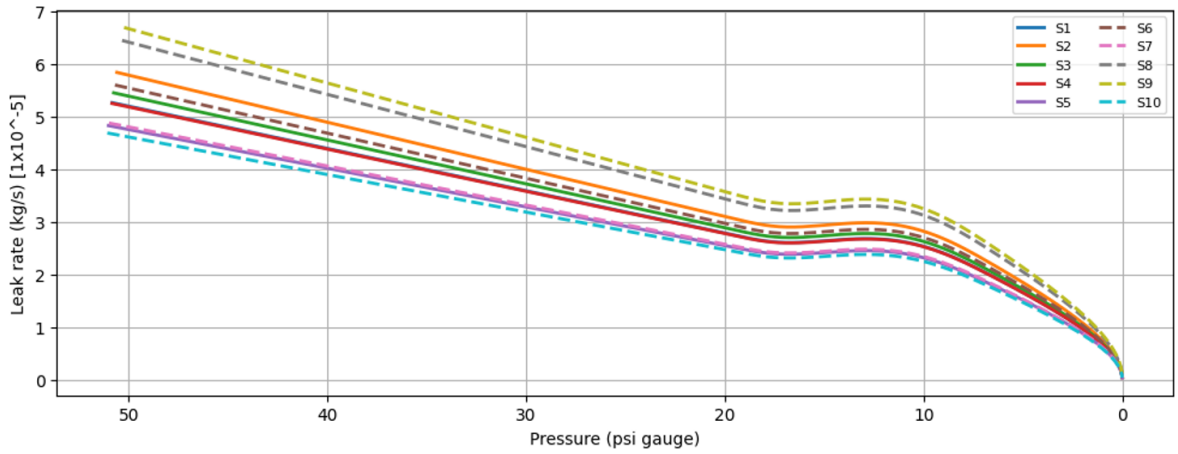

Figure 10. Leak rate vs. pressure profiled of the ten printed samples with leaks.

In addition to the previous quantitative leak detection studies, a complementary verification was achieved using an LED outcome on the ultrasonic system (see Figure 11). Here, the acoustic system acted as a binary classifier confirming leak presence. In the baseline condition (no air supplied to the part), the LED on the acoustic sensor remained green, indicating no detected ultrasonic emissions. When airflow was initiated and a leak existed, the LED transitioned to red, confirming acoustic activity produced by the gas escaping the part. Furthermore, when the system was tested with a printed sample without leaks, the LED remained steadily green. This acoustic based LED output provides a rapid qualitative leak confirmation that, in conjunction with the IR output, establishes a multi-modal detection platform.

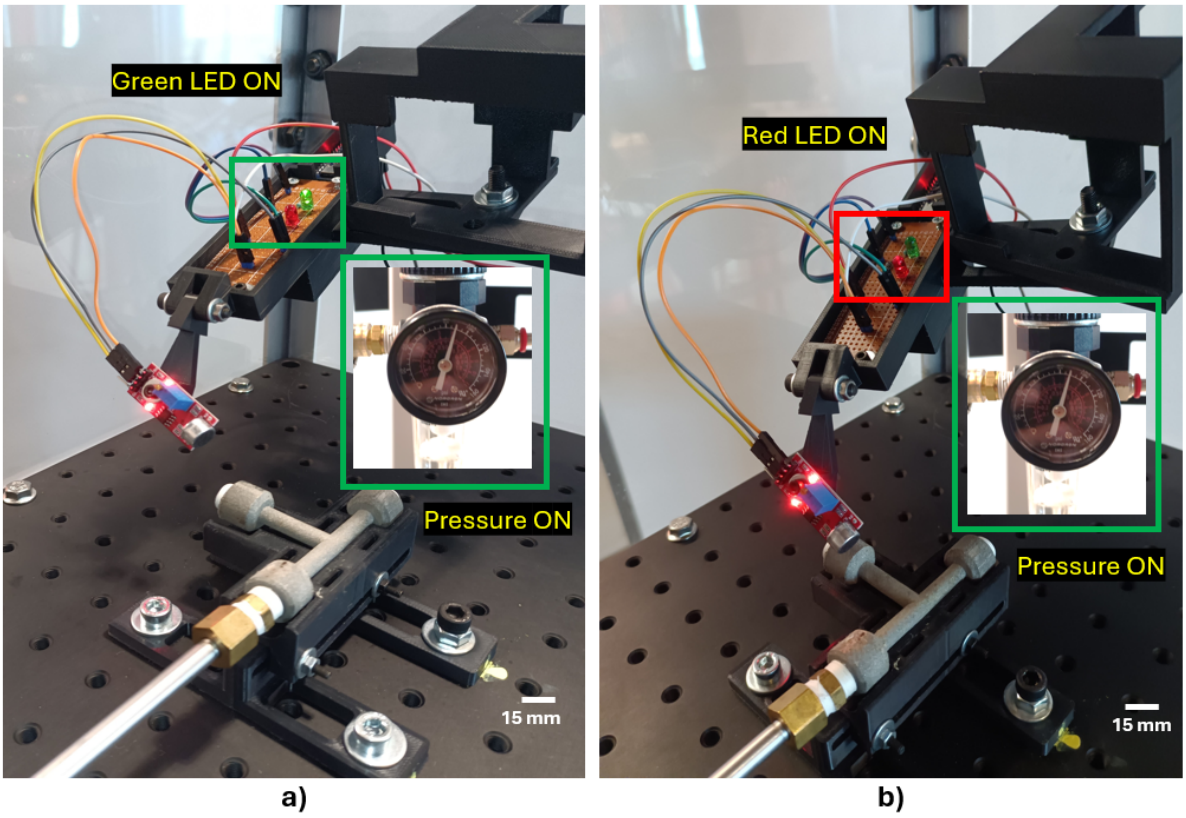

Figure 11. Modular NDE leak detecting sensor. (**a**) No detection of leak—green LED; (**b**) Detecting leak—red LED.

In addition to the baseline specimens, the modified-parameter sample and the reinforced specimen with increased wall thickness (+1 mm) were also evaluated using the ultrasonic detection system under identical pressurization conditions. In both cases, the recorded acoustic response remained below the established leak threshold throughout the testing interval, and no leakage was detected. These findings are consistent with the thermal imaging results and confirm the absence of through-wall defects. The agreement between infrared and ultrasonic measurements further supports the reliability of the proposed multimodal nondestructive evaluation platform across varying processing parameters and geometric configurations.

3.5. Computed Tomography (CT) Scan

To correlate the infrared and ultrasonic results with the internal conformation of the printed components, X-ray computed tomography (CT) analysis was performed on sectioned portions of the samples, as shown in Figure 12. The CT scan revealed a complex network of interconnected voids distributed within the pipe wall, confirming the presence of leakage paths identified in previous tests. The reconstructed slices show a continuous distribution of subsurface pores throughout the ring wall, with localized regions of pore clustering highlighted in yellow. These "hot-spot" regions correspond to areas where leakage was consistently detected. The presence of contiguous pore chains extending from the inner (4.06 mm diameter approx.) to the outer (6.40 mm diameter approx.) surface indicates the formation of through-wall pathways, providing direct qualitative evidence of subsurface connectivity responsible for leakage behavior.

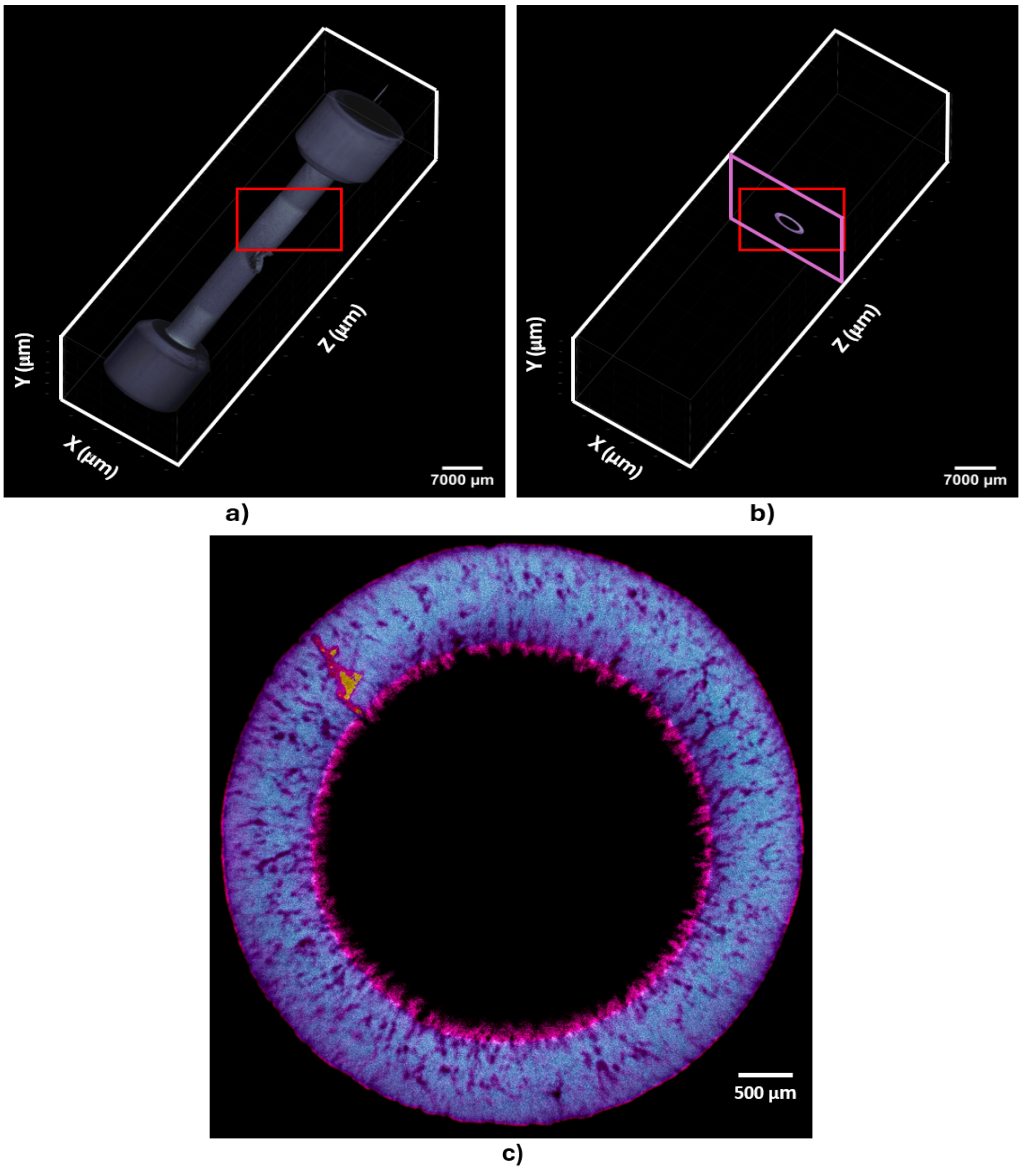

Figure 12. Scanned printed sample. (**a**) Longitudinal section of the part; (**b**) Sectioned layer for transversal analysis; (**c**) 2D image of the sectioned layer (red/yellow spots mark the void interconnection leak).

To further quantify the pore structure, high-resolution X-ray computed tomography (X-CT) analysis was conducted on the region of interest (ROI), as shown in Figure 13. The three-dimensional volume rendering reveals the spatial distribution of pores, which are color-mapped according to their equivalent diameter (some equivalent diameter based on clusters formed in certain areas). For quantitative consistency, only pores ≥ 60 µm (three times the voxel resolution) were included in the analysis. The majority of detected pores exhibited equivalent diameters below 300 µm, with a mean size of 101 ± 0.5 µm. A smaller population of larger defects, ranging from 300 to 990 µm, was also identified and is probably associated with the lack-of-fusion (LOF) defects. The volumetric pore size distribution across the whole structure is presented in Figure 14, confirming that these larger defects form the upper tail of the distribution. The overall material density derived from the X-CT analysis was 93.31%, indicating a significant presence of internal porosity within the whole structure.

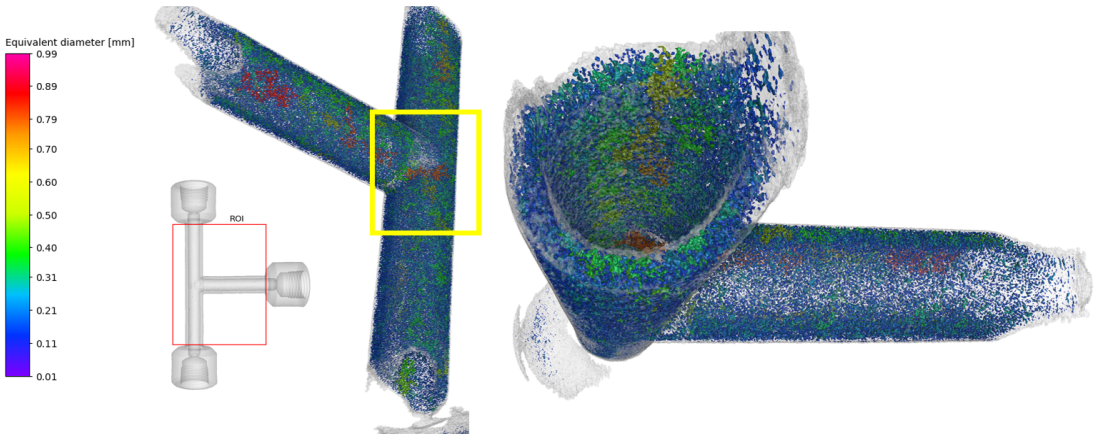

Figure 13. X-ray computed tomography (X-CT) volume rendering of the component showing the analyzed region of interest (ROI, **left**). Black box region confirms the leak detection area of the sample.

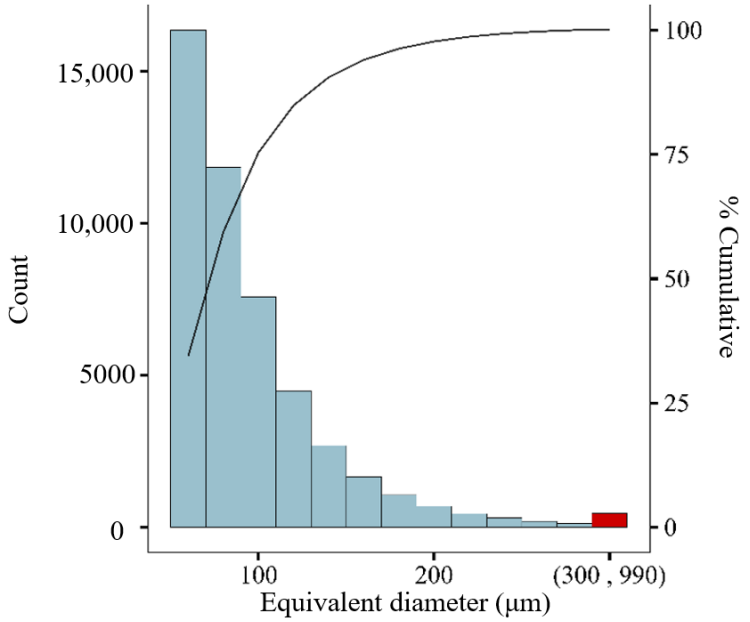

Figure 14. Volumetric based histogram of pore equivalent diameter (µm) with cumulative distribution (right axis) for X-CT–detected porosity (n = 47,895). Pores smaller than 60 µm were excluded based on resolution limits. Approximately 99% of pores are below 300 µm (D99 ≈ 290 µm), with a mean equivalent diameter of 101 ± 0.5 µm. The red bar (300–990 µm) highlights the small population of lack-of-fusion defects, which form the upper tail of the distribution. Quantiles are D25 = 70 µm, D50 = 90 µm, D75 = 120 µm, D90 = 160 µm, and D95 = 190 µm.

Combining qualitative and quantitative observations, the CT analysis provides direct three-dimensional confirmation of the transition from predominantly discrete porosity to interconnected pore networks within the pipe wall. While optical microscopy revealed a high density of near-surface voids, the CT results demonstrate that, at the measured porosity levels, these defects can link across successive layers and form continuous subsurface

pathways connecting the inner and outer surfaces. The spatial clustering of pores observed in the CT reconstruction correlates with the elbow region where leaks were consistently detected by thermal and ultrasonic methods, explaining the repeatable leak locations across samples. Furthermore, the presence of larger LOF-type defects contributes significantly to pore interconnectivity by acting as bridging features between smaller pores. These interconnected networks enable continuous gas transport, whereas more fragmented porosity restricts flow and results in reduced leakage rates. This relationship explains the variability observed in pressure decay behavior and confirms that leak formation in LPBF components is governed not only by pore size, but more critically by pore connectivity and spatial distribution.

4. Conclusions

The evaluation of LPBF printed 316L stainless steel components, confirmed the presence of both isolated and clustered micro voids that results in porosity. A process primarily associated with lack of fusion and gas entrapment. The Python code here used proved to be an effective post-process diagnostic and correlation tool for quantifying void size distribution, and spatial pore interconnectivity

Leak testing under internal pressure revealed the presence of leaks in defective samples. The acoustic testing based on ultrasonic frequency content enabled clear discrimination between background noise and active leakage events, confirming the presence of real through-wall defects. Furthermore, the measured sound intensity levels could allow for an estimation of the effective leak size through a calibration with known voids/defects. In parallel, pressure decay and leak rate analysis provided a quantitative assessment of the leakage profile. The combined interpretation of frequency, intensity, pressure decay, and flow rate data confirm that the observed defects are not merely superficial but represent structural critical leakage paths. These features directly compromise the performance of the components, particularly for applications requiring reliable pressure containment.

Thermal imaging and ultrasonic sensing successfully corroborated the locations of the detected leaks, consistently identifying the geometric regions across different specimen batches. The combined use of these nondestructive techniques proved highly effective for rapid leak localization and validation.

CT scan analysis revealed extensive interconnectivity of porosity across the layered structure of the LPBF samples. The scans demonstrated that voids were not isolated but instead formed interconnected networks throughout the material, enabling the development of continuous leakage pathways. This interlayer connectivity directly explains the persistent leaks detected during pressure testing and confirms the structural weakness induced by the manufacturing process.

The T-pipe samples analyzed in this study were fabricated using process parameters recommended by the LPBF system supplier, which are intended to provide robust and repeatable printing of 316L stainless steel across a wide range of geometries rather than to achieve geometry-specific optimization. While such parameter sets are commonly used as a baseline for industrial production, they do not necessarily minimize porosity in thin-wall or complex joint regions, such as the tee intersection investigated here. Variations in laser power, scan speed, and contour processing are known to influence melt pool stability, energy density distribution, and interlayer bonding, with insufficient local energy input promoting lack-of-fusion defects and excessive energy leading to alternative porosity mechanisms. In the present work, the supplier-recommended parameters enabled consistent fabrication of test samples while intentionally preserving manufacturing-induced defects representative of low-power (100 W) LPBF systems. This provided a realistic test case for evaluating the performance of the proposed multimodal nondestructive evaluation platform. Ongoing and future work will focus on a structured design-of-experiments (DOE) approach to parameter optimization, followed by re-evaluation of the nondestructive sensing system on optimized builds, thereby closing the loop between process optimization and defect detection capability.

In conclusion, this study demonstrates that a modular nondestructive platform integrated by an IR camera and an ultrasonic system could significantly improve real-time defect detection of pressurized components, enhance quality control, and ultimately increase the overall reliability of manufactured components.

Author Contributions

J.A.: conceptualization (lead), writing—original draft (lead), formal analysis (lead), writing—review and editing (lead); A.C.M.: review and editing (supporting); S.B.: resources (supporting); P.C.: methodology (lead), writing—review and editing (lead), supervision (lead); D.A.R.: writing—original draft (supporting), writing—review and editing (equal); C.B.A.: conceptualization (supporting), writing—original draft (supporting), writing—review and editing (equal); A.M.: conceptualization (supporting), writing—original draft (supporting), writing—review and editing (equal); E.M.: writing—review and editing (lead), validation—verification (lead); t.f.: formal analysis (supporting), resources (supporting), writing—review and editing; M.H.: formal analysis (supporting),

resources (supporting), writing—review and editing (supporting). All authors have read and agreed to the published version of the manuscript.

Funding

This research received no external funding.

Institutional Review Board Statement

Not applicable.

Informed Consent Statement

Not applicable.

Data Availability Statement

All relevant data supporting the findings of this study are included within the article.

Acknowledgments

The authors would like to acknowledge the support from and Murchison Endowment and Regent's Research Excellence Program from The University of Texas at El Paso. We are also grateful to Oak Ridge National Laboratory form their technical support. The authors also acknowledge the support from ConTex grant from The University of Texas System and Mexico's Secretariat of Science, Humanities, Technology, and Innovation (SECIHTI). The opinions expressed are those of the authors and do not necessarily represent views of these funding agencies.

Conflicts of Interest

The authors declare no conflict of interest.

Use of AI and AI-Assisted Technologies

No AI tools were utilized for this paper.

References

1. Bond, A.C.; Pohl, H.O.; Chaffee, N.H.; et al. Design Guide for High Pressure Oxygen Systems. NASA-RP-1113; NASA Lyndon B. Johnson Space Center, 1983. Available online: https://ntrs.nasa.gov/citations/19830024719 (accessed on 6 January 2026).
2. Kulor, F.; Markus, E.D.; Kanzumba, K. Design and Control Challenges of Hybrid, Dual Nozzle Gas Turbine Power Generating Plant: A Critical Review. *Energy Rep.* **2021**, *7*, 324–335. https://doi.org/10.1016/j.egyr.2020.12.042.
3. Oehlschlaeger, M.A. Grand Challenges in Aerospace Propulsion. *Front. Aerosp. Eng.* **2022**, *1*, 1027943. https://doi.org/10.3389/fpace.2022.1027943.
4. Cirrone, D.M.C. Hazards from Catastrophic Failure of High-Pressure Hydrogen Storage. Bachelor's Thesis, Ulster University, Belfast, Northern Ireland, 2018. Available online: https://pure.ulster.ac.uk/en/studentTheses/hazards-from-catastrophic-failure-of-high-pressure-hydrogen-stora (accessed on 6 January 2026).
5. Clausen, J.; Larsen, A.; Larsen, J.; et al. Disruption Management in the Airline Industry—Concepts, Models and Methods. *Comput. Oper. Res.* **2010**, *37*, 809–821. https://doi.org/10.1016/j.cor.2009.03.027.
6. Daga, R.; Samal, M.K. Real-Time Monitoring of High Temperature Components. *Procedia Eng.* **2013**, *55*, 421–427. https://doi.org/10.1016/j.proeng.2013.03.274.
7. Constantin, L.; Kraiem, N.; Wu, Z.; et al. Manufacturing of Complex Diamond-Based Composite Structures via Laser Powder-Bed Fusion. *Addit. Manuf.* **2021**, *40*, 101927. https://doi.org/10.1016/j.addma.2021.101927.
8. Singh, R.; Gupta, A.; Tripathi, O.; et al. Powder Bed Fusion Process in Additive Manufacturing: An Overview. *Mater. Today Proc.* **2020**, *26*, 3058–3070. https://doi.org/10.1016/j.matpr.2020.02.635.
9. Eliasu, A. Microstructural and Mechanical Integrity of 3D Printed 316L Stainless Steel. Master's Thesis, York University, North York, ON, Canada, 2020. Available online: https://yorkspace.library.yorku.ca/items/5b50882d-2fc2-4794-8a6f-e33f64829804 (accessed on 6 January 2026).

10. Mahmood, M.A.; Ishfaq, K.; Oane, M.; et al. Porosity Prediction in LPBF of AISI 316L Stainless Steel: Refined Volumetric Energy Density and FEM Simulation Approach. *Opt. Laser Technol.* **2025**, *188*, 113015. https://doi.org/10.1016/j.optlastec.2025.113015.
11. Honarvar, F.; Varvani-Farahani, A. A Review of Ultrasonic Testing Applications in Additive Manufacturing: Defect Evaluation, Material Characterization, and Process Control. *Ultrasonics* **2020**, *108*, 106227. https://doi.org/10.1016/j.ultras.2020.106227.
12. Chatillon, S.; Cattiaux, G.; Serre, M.; et al. Ultrasonic Non-Destructive Testing of Pieces of Complex Geometry with a Flexible Phased Array Transducer. *Ultrasonics* **2000**, *38*, 131–134. https://doi.org/10.1016/S0041-624X(99)00181-X.
13. Attallah, O. Multitask Deep Learning-Based Pipeline for Gas Leakage Detection via E-Nose and Thermal Imaging Multimodal Fusion. *Chemosensors* **2023**, *11*, 364. https://doi.org/10.3390/chemosensors11070364.
14. Yuan, F.; Zeng, Y.; Khoo, B.C. A New Real-Gas Model to Characterize and Predict Gas Leakage for High-Pressure Gas Pipeline. *J. Loss Prev. Process Ind.* **2022**, *74*, 104650. https://doi.org/10.1016/j.jlp.2021.104650.
15. Barber, R.; Rodriguez-Conejo, M.A.; Melendez, J.; et al. Design of an Infrared Imaging System for Robotic Inspection of Gas Leaks in Industrial Environments. *Int. J. Adv. Robot. Syst.* **2015**, *12*, 23. https://doi.org/10.5772/60058.
16. Kumpati, R.; Skarka, W.; Ontipuli, S.K. Current Trends in Integration of Nondestructive Testing Methods for Engineered Materials Testing. *Sensors* **2021**, *21*, 6175. https://doi.org/10.3390/s21186175.
17. Agarwal, A. An Investigation on Leakage Behaviour of Seals for Aerospace Applications. Master's Thesis, Delft University of Technology, Delft, The Netherlands, 2014. Available online: https://repository.tudelft.nl/record/uuid:04e3d6f0-a621-4bee-95ef-2c872628ffb2 (accessed on 6 January 2026).
18. Zaman, D.; Tiwari, M.K.; Gupta, A.K.; et al. A Review of Leakage Detection Strategies for Pressurised Pipeline in Steady-State. *Eng. Fail. Anal.* **2020**, *109*, 104264. https://doi.org/10.1016/j.engfailanal.2019.104264.
19. Zhu, P.; Liyanage, J.P.; Panesar, S.S.; et al. Review of Workflows of Emergency Shutdown Systems in the Norwegian Oil and Gas Industry. *Saf. Sci.* **2020**, *121*, 594–602. https://doi.org/10.1016/j.ssci.2019.02.037.
20. Santos, A.; Younis, M. A Sensor Network for Non-Intrusive and Efficient Leak Detection in Long Pipelines. In Proceedings of the 2011 IFIP Wireless Days (WD), Niagara Falls, ON, Canada, 10–12 October 2011; pp. 1–6. https://doi.org/10.1109/WD.2011.6098178.
21. Sonkar, S.K.; Kumar, P.; George, R.C.; et al. Detection and Estimation of Natural Gas Leakage Using UAV by Machine Learning Algorithms. *IEEE Sens. J.* **2022**, *22*, 8041–8049. https://doi.org/10.1109/JSEN.2022.3157872.
22. Lu, H.; Huang, K.; Azimi, M.; et al. Blockchain Technology in the Oil and Gas Industry: A Review of Applications, Opportunities, Challenges, and Risks. *IEEE Access* **2019**, *7*, 41426–41444. https://doi.org/10.1109/ACCESS.2019.2907695.
23. Papa, I.; Manco, E.; Epasto, G.; et al. Impact Behaviour and Non-Destructive Evaluation of 3D Printed Reinforced Composites. *Compos. Struct.* **2022**, *281*, 115112. https://doi.org/10.1016/j.compstruct.2021.115112.
24. Bayaniahangar, R.; Okoh, I.; Nawaz, K.; et al. Toward Extreme High-Temperature Supercritical CO_2 Power Cycles: Leakage Characterization of Ceramic 3D-Printed Heat Exchangers. *Addit. Manuf.* **2022**, *54*, 102783. https://doi.org/10.1016/j.addma.2022.102783.
25. Asadzadeh, S.; de Oliveira, W.J.; de Souza Filho, C.R. UAV-Based Remote Sensing for the Petroleum Industry and Environmental Monitoring: State-of-the-Art and Perspectives. *J. Pet. Sci. Eng.* **2022**, *208*, 109633. https://doi.org/10.1016/j.petrol.2021.109633.
26. Ho, M.; El-Borgi, S.; Patil, D.; et al. Inspection and Monitoring Systems for Subsea Pipelines: A Review Paper. *Struct. Health Monit.* **2019**, *19*, 606–645. https://doi.org/10.1177/1475921719837718.
27. Seifi, M.; Salem, A.; Beuth, J.; et al. Overview of Materials Qualification Needs for Metal Additive Manufacturing. *JOM* **2016**, *68*, 747–764. https://doi.org/10.1007/s11837-015-1810-0.
28. Najmon, J.C.; Raeisi, S.; Tovar, A. Review of Additive Manufacturing Technologies and Applications in the Aerospace Industry. In *Additive Manufacturing for the Aerospace Industry*; Froes, F., Boyer, R., Eds.; Elsevier: Amsterdam, The Netherlands, 2019; pp. 7–31. https://doi.org/10.1016/B978-0-12-814062-8.00002-9.
29. Dwivedi, S.K.; Vishwakarma, M.; Soni, A. Advances and Researches on Non-Destructive Testing: A Review. *Mater. Today Proc.* **2018**, *5*, 3690–3698. https://doi.org/10.1016/j.matpr.2017.11.620.
30. NASA. Standard for Stainless Steel Piping Systems AA, ACK1, ACK4, ACK6, B, BCK1, BCK3, BCK4, BCK6, BCK10, C, EE, G, H, JJ, K3, L1, L2, NCK1, NCK2, NCK3, NCK10, NCK11, NCK12, P, R, T, and Z. Available online: https://standards.nasa.gov/standard/SSC/SSTD-8070-0047-PIPE (accessed on 6 January 2026).
31. Sun, C.-N.; Aw, B.L.; Gu, H.; et al. Porosity Distribution of 316L Stainless Steel in Laser Powder Bed Fusion Additive Manufacturing Due to Spatial Variation. *J. Manuf. Process.* **2025**, *139*, 81–89. https://doi.org/10.1016/j.jmapro.2025.02.031.
32. Ronneberg, T.; Davies, C.M.; Hooper, P.A. Revealing Relationships between Porosity, Microstructure, and Mechanical Properties of Laser Powder Bed Fusion 316L Stainless Steel through Heat Treatment. *Mater. Des.* **2020**, *189*, 108481. https://doi.org/10.1016/j.matdes.2020.108481.

33. Snell, R.; Tammas-Williams, S.; Chechik, L.; et al. Methods for Rapid Pore Classification in Metal Additive Manufacturing. *JOM* **2020**, *72*, 101–109. https://doi.org/10.1007/s11837-019-03761-9.
34. Kim, F.H.; Moylan, S.P.; Garboczi, E.J.; et al. Investigation of Pore Structure in Cobalt Chrome Additively Manufactured Parts Using X-ray Computed Tomography and Three-Dimensional Image Analysis. *Addit. Manuf.* **2017**, *17*, 23–38. https://doi.org/10.1016/j.addma.2017.06.011.
35. Huang, X.; Yang, D.; Kang, Z. Impact of Pore Distribution Characteristics on Percolation Threshold Based on Site Percolation Theory. *Physica A* **2021**, *570*, 125800. https://doi.org/10.1016/j.physa.2021.125800.
36. Zurcher, T.; Fridrici, V.; Charkaluk, E. Surface Microstructure of an IN718 3D Coating Manufactured by Laser Metal Deposition. *Mater. Charact.* **2023**, *203*, 113054. https://doi.org/10.1016/j.matchar.2023.113054.
37. Pant, P.; Salvemini, F.; Proper, S.; et al. A Study of the Influence of Novel Scan Strategies on Residual Stress and Microstructure of L-Shaped LPBF IN718 Samples. *Mater. Des.* **2022**, *214*, 110386. https://doi.org/10.1016/j.matdes.2022.110386.
38. Yildiz, R.A.; Popa, A.-A.; Malekan, M. On the Effect of Small Laser Spot Size on the Mechanical Behaviour of 316L Stainless Steel Fabricated by L-PBF Additive Manufacturing. *Mater. Today Commun.* **2024**, *38*, 108168. https://doi.org/10.1016/j.mtcomm.2024.108168.
39. Smagowska, B.; Pawlaczyk-Łuszczyńska, M. Effects of Ultrasonic Noise on the Human Body—A Bibliographic Review. *Int. J. Occup. Saf. Ergon.* **2013**, *19*, 195–202. https://doi.org/10.1080/10803548.2013.11076978.